ADVANCED QUANTUM TECHNOLOGIES
www.advquantumtech.com

Transmission Spectroscopy of Molecular Spin Ensembles in the Dispersive Regime

Claudio Bonizzoni, Alberto Ghirri, Shigeaki Nakazawa, Shinsuke Nishida, Kazunobu Sato, Takeji Takui, and Marco Affronte*

The readout in the dispersive regime is originally developed—and it is now largely exploited—for non-demolitive measurement of super- and semiconducting qubits. More recently it has been successfully applied to probe collective spin excitations in ferro(i)magnetic bulk samples or collections of paramagnetic spin centers embedded into microwave cavities. The use of this readout technique within a semiclassical limit of excitation is only marginally investigated although it holds for a wide class of problems, including advanced magnetic resonance techniques. In this work, the coupling between a coplanar microwave resonator and diphenyl-nitroxide organic radical diluted in a fully deuterated benzophenone single crystal is investigated. Two-tone transmission spectroscopy experiments demonstrate the possibility to reconstruct the spectrum of the spin system with little loss of sensitivity with respect to the resonant regime. Likewise, pulse sequences of detuned microwave frequency allow the measurement of the spin-lattice relaxation time (T_1). The independent tunability of the probe and the drive power enables one to adjust the signal-to-noise ratio of the spectroscopy. These results suggest that electron spin dispersive spectroscopy can be used as a complementary tool of electron spin resonance to investigate the spin response.

1. Introduction

The problem of a two-level system (TLS) coupled to photons in a cavity plays a central role in quantum science and technologies[1] and it has been widely explored in resonance conditions and deeply exploited for techniques such as magnetic resonance spectroscopy. Residual coupling effects, with no direct exchange of energy between the two systems, are visible when the energy of the TLS is detuned with respect to the one of the cavity. While the details of this interplay may depend on the strength of the interaction and on the quantum or classical nature of the systems involved, the main effect consists in a shift in frequency and phase of the cavity mode conditioned by the state of the TLS. This interplay has been successfully exploited in circuit quantum electrodynamics (circuit QED) experiments performed in the so-called dispersive regime. In the pure quantum regime (i.e., a sole TLS interacting with a single or few photons in a cavity) the problem is described by the Jaynes–Cummings Hamiltonian, which can be naturally extended to the case of an ensemble of TLS interacting with the photon by the Tavis–Cummings model. Within this framework, the dispersive limit is achieved when the frequencies of the two systems (i.e., cavity and TLS) are largely detuned with respect to their mutual coupling rate. Over the last decades this regime has emerged as a powerful resource for quantum technologies thanks to the possibility for a cavity mode to interact with different quantum systems in a non-demolitive way,[2–4] performing the so-called dispersive readout. This was initially developed and applied to superconducting quantum bits[5] embedded into planar superconducting microwave (MW) resonators.[6–11] The possibility to preserve the

Dr. C. Bonizzoni, Dr. A. Ghirri, Prof. M. Affronte
CNR Istituto Nanoscienze
Centro S3, via G. Campi 213/A, Modena 41125, Italy
E-mail: claudio.bonizzoni@unimore.it

The ORCID identification number(s) for the author(s) of this article can be found under https://doi.org/10.1002/qute.202100039

†This work is dedicated to the memory of Dr. Shigeaki Nakazawa, who deceased on March 23, 2019.

DOI: 10.1002/qute.202100039

Dr. S. Nakazawa†, Dr. S. Nishida, Prof. K. Sato, Prof. T. Takui
Department of Chemistry and Molecular Materials Science
Graduate School of Science
Osaka City University
3-3-138 Sugimoto, Sumiyoshi-ku, Osaka 558-8585, Japan

Prof. T. Takui
Japan and Research Support Department/University Research Administrator Center
University Administration Division
Osaka City University
3-3-138 Sugimoto, Sumiyoshi-ku, Osaka 558-8585, Japan

Prof. M. Affronte
Dipartimento di Scienze Fisiche Informatiche e Matematiche
Università di Modena e Reggio Emilia
via G. Campi 213/A, Modena 41125, Italy

quantum features during the measurement brought the application of this approach also in spectroscopic experiments, for example, to measure the anharmonic energy levels of superconducting qubits[12,13] or to perform gate reflectometry of an electron spin in semiconductor quantum dots.[14–16] On the other way around, the dispersive regime has been used also as part of the experimental protocols for the detection of single or few microwave photons through superconducting qubits.[17–21]

More recently, the dispersive regime has been also applied for studying collective bosonic excitations, in particular collective spin modes coupled to microwave ones. Here the attention is focused on long lifetime excitations of the ensemble. Along this line, detection of single magnonic excitations was demonstrated in low temperature dispersive experiments performed on (ferri)magnetic yttrium iron garnet (YIG) spheres coupled to 3D resonant cavities.[22] Paramagnetic spin ensembles of nitrogen vacancy (NV) centers in diamond were also studied in the dispersive limit leading to an alternative measurement scheme for the spin-lattice relaxation time T_1, from room temperature[23] down to the Purcell-limited regime,[24] and for the spectral density of the NV centers.[25,26] Interestingly, the dispersive interplay is found to persist also in a semiclassical regime (i.e., large collection of TLSs interacting with a large number of photons, giving a classical regime of excitation for MW field) thus allowing the observation and the exploitation of its effects at room temperature.[23,27]

Molecular spins have recently emerged as promising systems for quantum technologies. Here the interest is given by the relatively long memory time achievable over a wide temperature range[28–30] which makes them suitable for encoding quantum bits[31–33] and for quantum sensing.[34] The coherent spin-photon coupling between the resonators and concentrated ensembles of organic radicals (DPPH and PyBTM)[35–37] and with transition-metal oxovanadyl (VOPc)[38,39] has been demonstrated. Moreover, the coherent manipulation of molecular spin ensembles through planar resonators with sequences of MW pulses has been recently shown.[40] Nonresonant state readout of single molecule magnet (Ni_4) by a microstrip resonator was proposed,[41] while a first study on a tetrathiafulvalenes organic radical microcrystal in the dispersive regime has been reported only recently.[42] Here we focus on diphenyl-nitroxide (DPNO) organic radical, whose interest is given by the possibility to functionalize these molecules and realize multiple client qubits on each of them.[43,44]

We report an extensive investigation on the dispersive regime achieved between a 1.5% diluted crystal of DPNO molecular spin ensemble and a superconducting coplanar microwave resonator at low temperature (2 K). We first briefly review the theoretical models behind the dispersive readout and we use them to demonstrate that the phenomenology observed in our experiments corresponds to the one expected from a two-tone continuous-wave (CW) microwave transmission spectroscopy in the dispersive limit. We finally test our readout scheme in the pulsed-wave (PW) regime, by measuring the spin-lattice relaxation of our samples. Our results suggest that an electron spin dispersive spectroscopy can be a complementary tool with respect to electron spin resonance (ESR) in the characterization of magnetic samples.

2. Description of the Dispersive Regime

We consider the interaction of an ensemble of N spins s coupled to a photon mode (resonant frequency ν_0) within the Tavis–Cummings model, whose Hamiltonian reads as[22,45–48]:

$$H = h\nu_0 a^\dagger a + h\nu_S b^\dagger b + h\Omega\left(a^\dagger b + a b^\dagger\right) \tag{1}$$

Here $a^\dagger$, a are the creation and annihilation operators of the photon in cavity (resonator), respectively, while $b = 1/\sqrt{2sN}\sum_i^N S_i^+$ is the collective annihilation operator for the spin ensemble, which is defined starting from the raising operator of the single spin (S_i^+). $\nu_S = g\mu_B B_0/h$, with g the Landé g-factor and μ_B the Bohr magneton, is the Zeeman energy of the spin ensemble, which can be tuned by the externally applied static magnetic field B_0. $\Omega = \Omega_S\sqrt{N_{\text{eff}}}$ is the collective coupling rate of the ensemble, which depends by the single spin-photon coupling rate Ω_S and by the effective number of spins coupled by the resonant mode, N_{eff} (this latter one being $N_{\text{eff}} \leq N$, depending on the temperature-dependent spin polarization). Equation (1) describes the coherent exchange of a single photon between the resonator and a collective excitation of the ensemble.[35,36,45,46,49,50] We just mention here that the Holstein–Primakoff[51] and the rotating wave approximation have been used. These approximations hold as far as the number of excitations of the system is much lower than the number of coupled spins (photon number $n \ll N, N_{\text{eff}}$)[45,49,52] and since the coupling rate between the two systems is much smaller than their bare transition energies.[45,50]

The dispersive limit of Equation (1) is defined by the condition $|\Delta| = |\nu_S - \nu_0| \gg \Omega$, and the Hamiltonian now takes the form:

$$H = h(\nu_0 - \chi)a^\dagger a + h(\nu_S + \chi)b^\dagger b + \frac{2}{N}\chi a^\dagger a b^\dagger b \tag{2}$$

where the dispersive shift χ is defined as:

$$\chi = \Omega^2/\Delta = \Omega_S^2 N_{\text{eff}}/\Delta \tag{3}$$

The last term of Equation (2), due to our large spin numbers, can be neglected. One can also see that two dressed energies can be defined as $\widetilde{\nu}_0 = \nu_0 - \chi$ and $\widetilde{\nu}_S = \nu_S + \chi$ for the resonator and the spin ensemble, respectively. A shift of the resonator energy is expected and, at the same time, the spin energy undergoes a shift with opposite sign. Moreover, Equation (3) shows that the the dispersive shift scales as the inverse of the detuning Δ and that it can be positive or negative depending on the sign of Δ. It also follows that, for fixed detuning and single spin coupling, the only way to change the dispersive shift value relies on the capability to change the effective number of spins N_{eff}, that is, to induce a change in the population difference between the energy levels of the ensemble (so, in the magnetization of the ensemble).[42] However, note that a similar expression for the first term of Equation (2) can be found also when nonlinear terms are introduced in the Hamiltonian by considering, for instance, multi-photon processes, interactions between magnetic modes or the presence of anharmonic energy levels of superconducting qubits. According to the seminal work of Imamoglu,[53] in these cases the strength of the shift χ is proportional to $\Omega_S^2 N_{\text{eff}}$ due to the fact that the spin

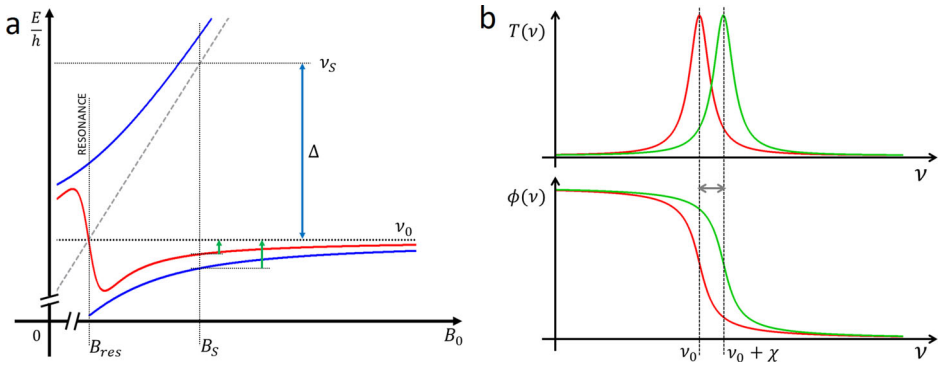

Figure 1. a) Map of the transition frequency as a function of the static magnetic field for the strong (blue) and the weak (red) coupling regime between spins and resonator. Black horizontal dotted line is the resonator frequency (ν_0), while the dashed gray line is the spin (Zeeman) energy. The resonance between the spins and the resonator occurs at B_{res} (vertical dashed line with label). The dispersive limit is achieved by the setting the magnetic field to B_S, corresponding to ν_S and to the detuning $\Delta = \nu_S - \nu_0$ (blue vertical arrow). The dispersive shift observed when the drive is tuned to ν_S corresponds to the green arrows. Note that here only the part of the map corresponding to $\Delta > 0$ is shown, and that the plot is not in scale to better highlight the shifts. $\chi > 0$ is also assumed. b) Simulation showing the shift of the transmission and of the phase of the resonator expected when the drive is turned on (green traces) with respect to the drive-off case (red traces). Here the we assume $\chi > 0$, $\Delta > 0$ so the resonator is blue-shifted.

ensemble responds collectively even in the limit of a single/few excitation(s).[22,42,45,46]

The energy shift of the resonator can be detected in both transmission and phase signals of the resonator (**Figure 1**). These can be modeled according to the input/output formalism,[36] while the following expression for the phase shift of the resonator, $\Delta\phi$, it is commonly used:

$$\Delta\phi = \arctan\left(\frac{2\chi}{\kappa}\right) \tag{4}$$

in analogy to what is typically done for superconducting qubits.[6] Here κ is the total decay rate of the resonator.

Equation (2) can be further extended to include the effect of an additional drive tone acting on the spin ensemble (see Section S1, Supporting Information). Here it is worth noting that the number of spin excitations is found to linearly increase with the MW drive power $P_{\mathrm{in,D}}$, while the signal amplitude is expected to scale linearly with the MW magnetic field $B_1 \propto \sqrt{P_{\mathrm{in,D}}}$. In this framework, a critical photon number can be also defined as $n_c = \Delta^2/(4\Omega_S^2)$[54,55] and it is found to depend on the single spin coupling rate.

We now revisit the results above under a semiclassical approach, in which the electromagnetic field generated by the resonator is treated classically. This situation is realized when the resonator is populated by a large number of photons. In addition, we consider the case in which the spin ensemble is weakly coupled to the MW photons, so no spin-photon hybridization (blue lines in Figure 1a) occurs. Under these conditions the dispersion of the resonator frequency takes places near the resonator frequency ($\nu_0 \approx \nu_S$, red line of Figure 1a) as an effect of the real part of the magnetic susceptibility.[56] Here the coupling between the spin ensemble and the electromagnetic field in a cavity or a resonator can be modeled as a lumped-element equivalent electrical network[57,58]:

$$\nu_0' = \nu_0 + \frac{\Omega^2(\nu_0 - \nu_s)}{(\nu_0 - \nu_s)^2 + \gamma^2} \tag{5}$$

Equation (5) describes the frequency of the resonator under the effect of the coupling with spins. Again, $\Omega = \Omega_S\sqrt{N_{\mathrm{eff}}}$ is the collective coupling rate, while γ is the ensemble decay rate, which corresponds to the half width at half maximum of the spin spectral density. The dispersive limit of Equation (5) only needs the detuning to be much larger than the spin linewidth ($\Delta > \gamma > \Omega$), that is, to use one of the tails of the energy dispersion (see Figure 1a). Hence, the dispersive limit is given by the limit of Equation (5) for $\Delta \to \infty$ (which corresponds to a Laurent series expansion):

$$\nu_0' = \nu_0 - \frac{\Omega^2}{\Delta} + \frac{\Omega^2\gamma^2}{\Delta^3} - \frac{\Omega^2\gamma^4}{\Delta^5} \approx \nu_0 - \chi \tag{6}$$

The terms of Equation (6) beyond the first order are expected to give vanishing contributions due to the large values of Δ. This way, at the first order the resonator is shifted by:

$$\nu_0' - \nu_0 = \chi \propto \Omega^2 \propto \Omega_S^2 N_{\mathrm{eff}} \tag{7}$$

with respect to its bare energy, as for Equation (3). This shows that also in the detuned weak coupling regime a shift of the resonator frequency is expected as a counterpart of the dispersive regime.[23,55,59] Here we note that an expression similar to Equation (6) can be derived also for the resonator decay rate (see Section S1, Supporting Information). As for Equation (3), the sign of the shift depends on the sign of the detuning, by the single spin coupling rate and the effective number of spins. We note, however, that the opposite shift of the spin energy ($\tilde{\nu}_S$, see above) is not expected. In other words, due to the weak coupling regime, it is not possible to probe the MW field of the resonator through the spins. Finally, according to the Bloch equations, the response of the spins is expected to be proportional to the applied MW magnetic field, as for the quantum regime.[56,60] This suggests that also in the weakly coupled dispersive limit (defined by $\Delta \gg \Omega$), effects on the energy of the resonator are expected. This situation corresponds to a transmission spectroscopy of the spin ensemble which, differently from ESR spectroscopy,

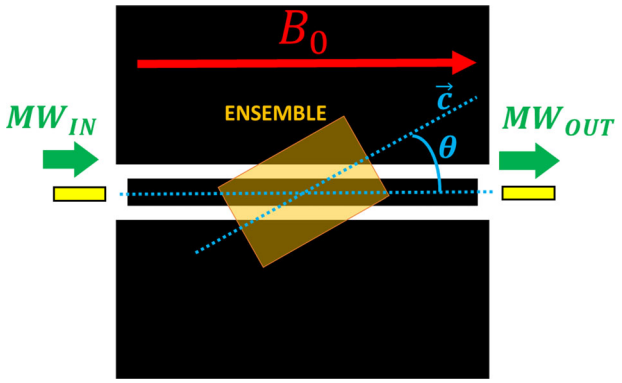

Figure 2. Sketch of the coplanar resonator used in the experiments. The resonant strip (width $w = 200\,\mu m$, length $L = 8$ mm) is the central rectangle, while additional ground planes are present on the two sides (side gap $s = 73\,\mu m$). Two tunable antennas (yellow) are used to couple the resonator to the feed lines. Green arrows shows the direction of the MW signal. Red arrow shows the externally applied magnetic field. The spin ensemble (orange) is placed in the middle of the resonant strip. If not otherwise specified, the crystal samples will be placed on the resonator and θ will be the angle between the c-axis and the direction of the static magnetic field. Further details on the resonator are given in Section 5.

is performed with the cavity detuned from the energy of the spins.

3. Experiments

We have performed a continuous-wave two-tone transmission spectroscopy on a fully deturated benzophenone–d_{10} single-crystal host containing a stable DPNO organic radical with 1.5% concentration (see Section 5). The crystal is placed on a superconducting coplanar resonator to couple to the magnetic field component $\mathbf{B}_1$ of the fundamental mode of the resonator ($\nu_0 = 7.74$ GHz, see Section 5), as in **Figure 2**. An external static magnetic field $\mathbf{B}_0$ is applied along the longitudinal axis of the strip to tune the spin energy far from the resonance, thus meeting the condition for the dispersive regime ($|\Delta| = |\nu_S - \nu_0| \gg \Omega$). The experimental set-up used is shown in **Figure 3**. A MW tone (hereafter, drive) generated by a MW source at ν_D is used to excite the spin ensemble around its Zeeman frequency, while a vector network analyzer (VNA) is used to generate a second MW tone (hereafter, probe), to monitor the transmission peak and phase of the resonator and to detect its frequency shift (see Section 5 for details).

3.1. Dispersive Shift of the Resonant Frequency

We first consider the dispersive shift induced by the DPNO sample on the resonator and compare its features to the model discussed in Section 2. Since the spin-resonator detuning has to be much larger than the coupling rate, we choose $|\Delta| = |\nu_S - \nu_0| \approx 420\,\text{MHz} \approx 53\,\Omega \gg \Omega$ as initial working condition (see Section S3, Supporting Information). This gives $\nu_S \approx 8.17$ GHz corresponding, for $g \approx 2$, to an externally applied static magnetic field $B_0 = 0.2900$ T. With these values the expected dispersive shift is $\chi = \Omega^2/\Delta \approx 0.12 \pm 0.1$ MHz. We first look at the transmission and at the phase of the resonant peak when the MW drive is ON or OFF at $\nu = 8.17$ GHz. A clear frequency shift of the resonant frequency is visible in **Figure 4** in both transmission and phase when the drive is turned ON. A similar measurement at 0 T gives no shifts, confirming that this effect is given by the interaction with the spins.

3.2. Comparison between Resonant and Dispersive Spectroscopy

We perform a two-tone transmission spectroscopy in the dispersive limit by acquiring the transmission and phase signal of the resonator for different drive frequencies at a fixed magnetic field value and we compare it with the results obtained in a single-tone resonant transmission spectroscopy.

Figure 5 shows the single-crystal transmission spectra measured as a function of the static magnetic field in a single-tone transmission spectroscopy in the resonant regime (red traces) for $\theta = 90°$ (a) and $\theta = 0°$ (b). For $\theta = 90°$, a central strong peak is visible along with two additional weaker ones on the two sides. Conversely, for $\theta = 0°$ three main lines with equal intensity are observed. Single-tone transmission spectroscopy shows that the sample is in the weak spin-photon coupling regime for both crystal orientations. High cooperativity regime can be achieved on larger crystals (see Section 3, Supporting Information). Further analysis of the single-tone resonant spectra and complementary simulations reveal that the spectra arise from the contribution of four different molecular orientations (see Section S2, Supporting Information). Figure 5a,b show the transmission shift of the resonator measured within the two-tone transmission spectroscopy in the dispersive regime (blue traces). To better compare the spectra with their corresponding single-tone ones we rescale the axes as follows. We first rescale the vertical axis of the dispersive spectrum and refer its baseline to zero to better fit with the single-tone transmission scale. We then convert the horizontal drive frequency scale to an equivalent magnetic field one in two steps: we first calculate the magnetic field values corresponding to the drive frequency with $B_{0,D} = h\nu_D/(g\mu_B)$ (which are around the chosen B_S and detuned from B_{res}) and we then scale-down these values to the resonant frequency of the resonator according to $B_{0,\nu 0} = B_{0,D}\,\nu_0/\nu_D$. In this way we obtain an equivalent magnetic field scale corresponding to the values probed by the drive frequency. For both the crystal orientations, the spectroscopic features found with two-tone measurements are consistent with the ones found with the single-tone spectroscopy, suggesting that the dispersive readout technique is effectively addressing the same transitions of the sample. Moreover, a closer look to the dispersive spectra for $\theta = 90°$ reveals that the signal, in particular the central one, results from the convolution of multiple signals. This is more evident for $\theta = 0°$, where up to six peaks are clearly visible with respect to the only three given by the single-tone spectroscopy.

In Figure 5c,d we compare the dispersive shifts measured in transmission ($\Delta|S_{21}|$, c) and phase ($\Delta\phi$, d) for both orientations as a function of the drive frequency. We also add the results obtained under similar conditions without the application of the MW drive tone, in which no shifts are expected (gray dashed lines). The change of the spectroscopic features with the orientation of the sample is clearly visible, consistently with the one observed in the CW single-tone resonant spectroscopy (see

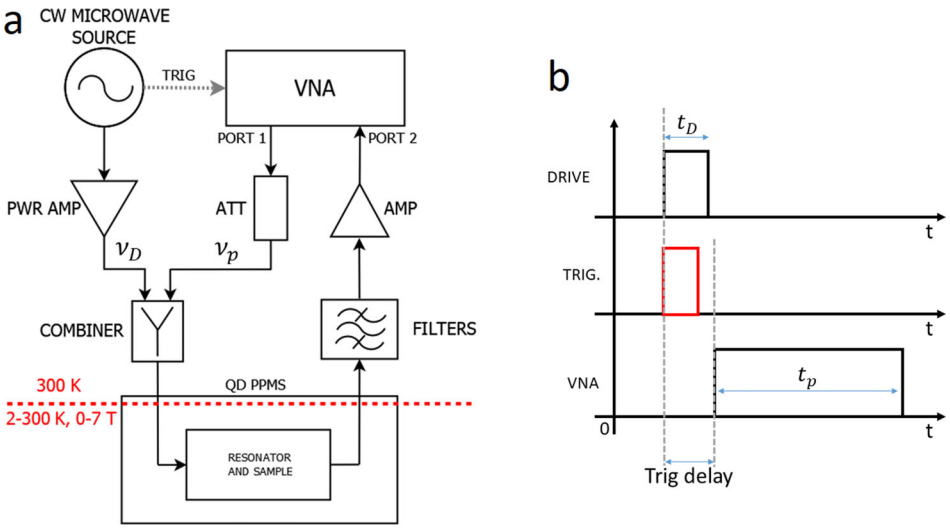

Figure 3. a) Scheme of the set-up for dispersive readout. The drive tone for the spin ensemble (ν_D) is generated by a microwave source, while the probe tone of the resonator (ν_p) is generated by a vector network analyzer (VNA), which is also used for the acquisition of the transmission and the phase of the resonator. The two tones are routed into the same MW input line with a power combiner. Additional amplification and attenuation stages are added to change the powers of the drive and of the probe tone. The trigger signal from the MW source to the VNA (gray dashed arrow) is used only in the pulsed-wave mode. b) Sketch of the pulse pattern used for the measurement of the energy relaxation (the horizontal axis and the pulse lengths are not in scale). Further details on the resonator are given in Section 5.

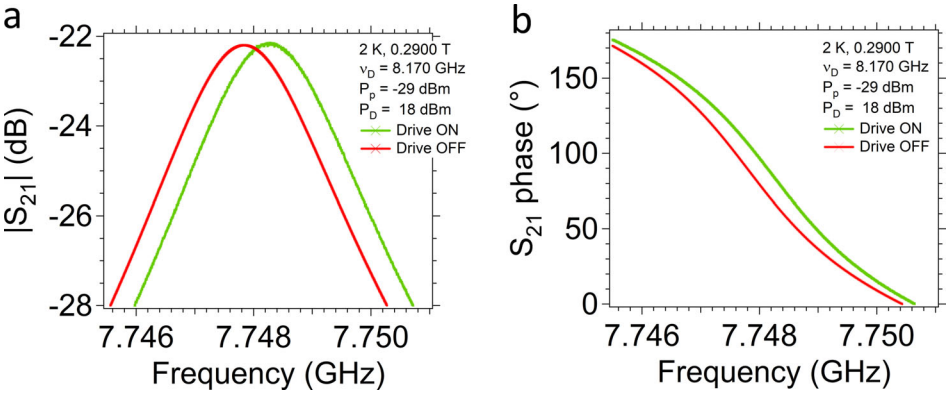

Figure 4. Dispersive shift of a) transmission and b) phase of the resonator measured for the DPNO spin ensemble at 2 K, $B_0 = 0.2900$ T, and for $\theta = 90°$ when the MW drive is turned ON (green trace) or kept OFF (red trace) at $\nu_S = 8.1705$ GHz. Probe and drive powers are $P_{\text{in,p}} = -29$ dBm and $P_{\text{in,D}} = +18$ dBm, respectively.

Figure S4, Supporting Information). The results show that, under our experimental conditions, it is possible to use either the phase and the transmission of the resonator to indirectly measure the spin ensemble, according to what predicted by Equations (7) and (4).

3.3. Dependence on Applied Microwave Power

Using two different MW tones allows us to investigate the effects of the probe and the drive power separately.

3.3.1. Dependence on the Drive Tone Power

The dependence of the dispersive signal on the input drive power is shown in **Figure 6**a,b. The intensity of the three peaks is found to increase when the larger power is applied, as also reported in refs. [27, 55]. As previously discussed, increasing the MW magnetic field associated to the drive tone increases the component of the magnetization in the precession plane with respect to the quantization axis.[56] To verify this, we extract the amplitude of peak #2 and we plot it as a function of the square root of the magnitude of the drive power $\sqrt{P_{\text{in,D}}} \propto B_1$ (Figure 6b). Data show a nice linear dependence, as corroborated also by the linear fit (green dashed line). A similar dependence is also found for peak #1 and #3 (see Figure S10, Supporting Information) thus confirming the expected linearity with the MW magnetic field strength.[56,60]

3.3.2. Dependence on the Probe Tone Power

While changing the drive power changes the intensity of the measured shift, changing the probe power is not expected to change

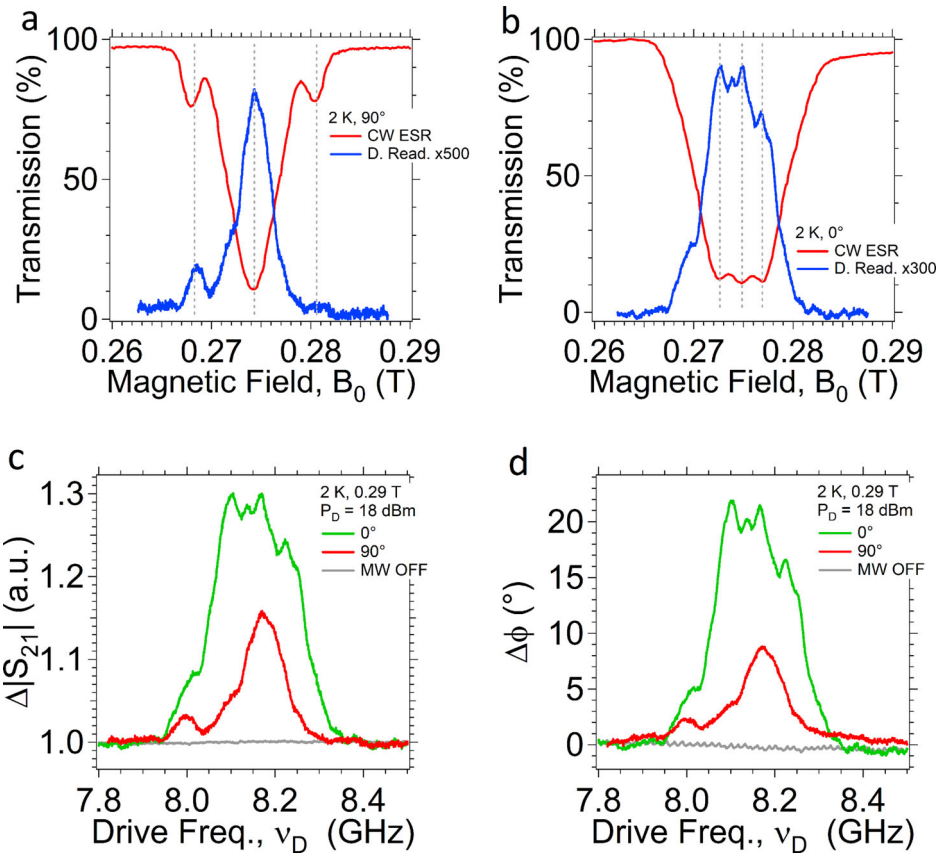

Figure 5. Top: Comparison between the dispersive shift of the transmission (blue) and the signal measured in a single-tone spectroscopy (red, see also Figure S4, Supporting Information) for a) $\theta = 90°$ and b) $\theta = 0°$. For the dispersive data the vertical axis has been rescaled for better comparison and the horizontal axis is an equivalent magnetic field scale covering the drive frequency range. The blue traces correspond to the dispersive shifts measured by setting the static magnetic field to $B_0 = 0.2900$ T. Bottom: Dispersive shifts of c) transmission and d) phase of the resonator measured for two different orientations of the *c*-axis of the 1.5% DPNO crystal with respect to the static magnetic field at 2 K and $P_{in,p} = -34$ dBm. The static magnetic field was set to $B_0 = 0.2900$ T, giving $\nu_S \approx 8.173$ GHz and $\Delta \approx 420$ MHz. The signal measured with the MW drive turned off at the same temperature and probe power (gray) is also reported.

the magnitude of the dispersive shift under our experimental conditions. Figure 6c,d show the results for $\theta = 90°$. The power of the probe tone can be changed over a range of up to $\approx$ 20 dB without significant alteration of the signal amplitude. The probe power can be as high as −30 dBm, a value at which the sample would begin to show a saturation of the lines (see Section S3, Supporting Information). As can be clearly seen in Figure 6d, the signal-to-noise ratio (SNR) of each trace is progressively improved with the increase of the probe power. This is due to the larger power probing the resonator, which improves the SNR of its transmission and the possibility to resolve the dispersive shift. For large enough detuning with respect to the resonator decay rate, the shape of the transmission of the resonator prevents the probe power from reaching the sample, protecting it from saturation and from possible cross-talks between the two MW tones. Additional results are reported in Figures S11 and S12, Supporting Information).

The mean photon number associated to the probe and to drive tone can be estimated (see Section S5, Supporting Information for details). Under our experimental conditions a probe power $P_{in,p} = -35$ dBm corresponds to $n_p \approx 10^9$ average photons populating the resonator, while a drive power $P_{in,D} = +18$ dBm corresponds to $n_D \approx 10^{10}$ photons reaching the spin ensemble. These large photon numbers justify the use of a classical description of the MW field of the resonator although, as discussed in Section 2, the phenomenology observed in the shift of the resonant frequency is perfectly equivalent to the one expected from the dispersive regime of the Tavis–Cummings Hamiltonian. Moreover, we note that the effective number of spins in our DPNO samples is $N_{eff} \approx 10^{14} - 10^{16}$ which is much larger with respect to both n_p, n_D, providing that our samples are in the regime of low number of excitations.[49] In addition, we note that the critical photon number under our experimental conditions is $n_c \approx 10^{17}$ (see Section S8, Supporting Information) that is much larger than both n_p, n_D, and N_{eff}, thus neither the dependence of the dispersive shift on the probe power or the appearance of nonlinear effects is expected.[4,45,53]

3.4. Dependence on Static Magnetic Field

3.4.1. Oddity of the Dispersive Shift with Respect to the Detuning

In **Figure 7**a,b we check the reversal of the dispersive signal with the sign inversion of the detuning (Equation (7)). We consider the

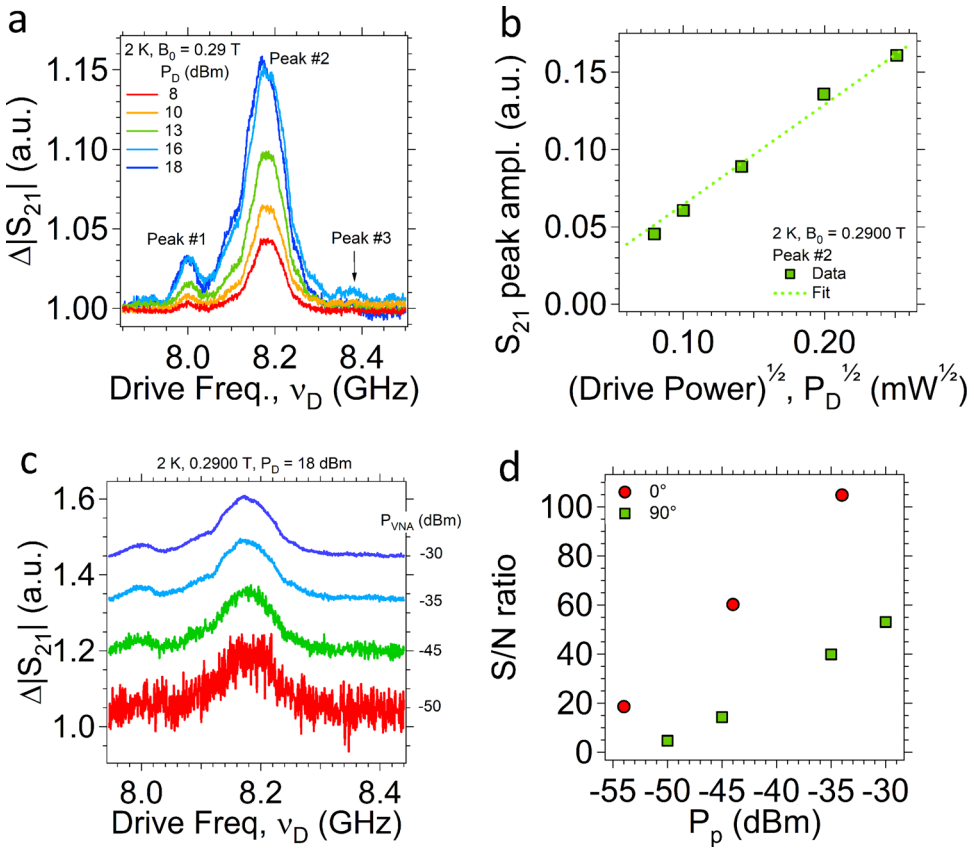

Figure 6. Top: a) Dispersive shift of the transmission measured for the 1.5% DPNO crystal at $B_0 = 0.2900$ T, 2 K, $P_{p,in} = -34$ dBm for $\theta = 90°$ and for different drive powers (see legend). Labels help in recognizing the three peaks. b) Transmission values extracted from the maxima of peak #2 of (a) as a function of the square root of the drive power. Dashed line is a linear fit. Bottom: c) Dispersive shifts of the transmission for DPNO crystal at $\theta = 90°$ as a function of the drive frequency for different probe powers (see labels). The data are plotted with vertical off-set for clarity. The temperature, the static magnetic and the drive power are indicated in the legend. d) Signal-to-noise ratio estimated from the signal corresponding to the main peak in (c) as a function of the probe power (green points). The points for the $\theta = 0°$ orientation calculated for the peak at 8.103 GHz are added for comparison (see Figure S12, Supporting Information).

shift of the transmission signal (a) and its phase (b) as a function of drive frequency for $\Delta = 700$ MHz ($B_0 = 0.3000$ T, green traces and axes) and for $\Delta = -700$ MHz ($B_0 = 0.2498$ T, red traces and axes). The horizontal axis is shifted for immediate comparison. The structures corresponding to $\Delta < 0$ now appear as dips in the baseline (negative shifts), confirming the reversal of the dispersive shift with respect to the $\Delta > 0$ case.

3.4.2. Dependence of the Dispersive Signal on Detuning

According to Equation (3), the dispersive shift depends on the reciprocal of the detuning $\Delta^{-1} = (\nu_S - \nu_0)^{-1} \propto (B_0 - B_{res})^{-1}$, B_{res} being the magnetic field at which the resonance with the resonator occurs. This dependence was checked by measuring the dispersive shift given by the DPNO sample as a function of the drive frequency for different static magnetic fields. The results are shown in Figure 7c. The transmission shift (peak #2) is visible for all the B_0 values while its intensity decreases with the increase of the detuning. Similar results are found also for the phase signal (Figure 7d) and for $\theta = 0°$ (see Figure S13, Supporting Information). Equation (4) was used to estimate the dispersive shift of peak #2 from its phase shift and we plot it as a function of the inverse of the difference $\Delta B^{-1} = (B_0 - B_{res})^{-1}$ (with $B_{res} = 0.2747$ T, see Section S3, Supporting Information,). Data of Figure 7 fit well the following expression (dashed line):

$$\chi = \frac{\Omega^2}{\Delta} = \frac{h\Omega^2}{g\mu_B(B_0 - B_{res})} = \frac{h\Omega^2}{g\mu_B}\Delta B^{-1} \quad (8)$$

which is based on Equation (3). This gives a collective coupling rate $\Omega = 7.0 \pm 0.5$ MHz that is consistent with what expected for this orientation (see above and Section S3, Supporting Information).

3.5. Dispersive Readout in the Pulsed-Wave Regime

The dispersive spectroscopy can also work in the pulsed-wave (PW) mode: a single MW drive pulse is used to excite the spins detuned from the resonator, while a long probing pulse is used to monitor the transmission and the phase of the resonator immediately after the MW drive pulse is sent (Figure 3b). The details on the PW protocols are given in Section 5.

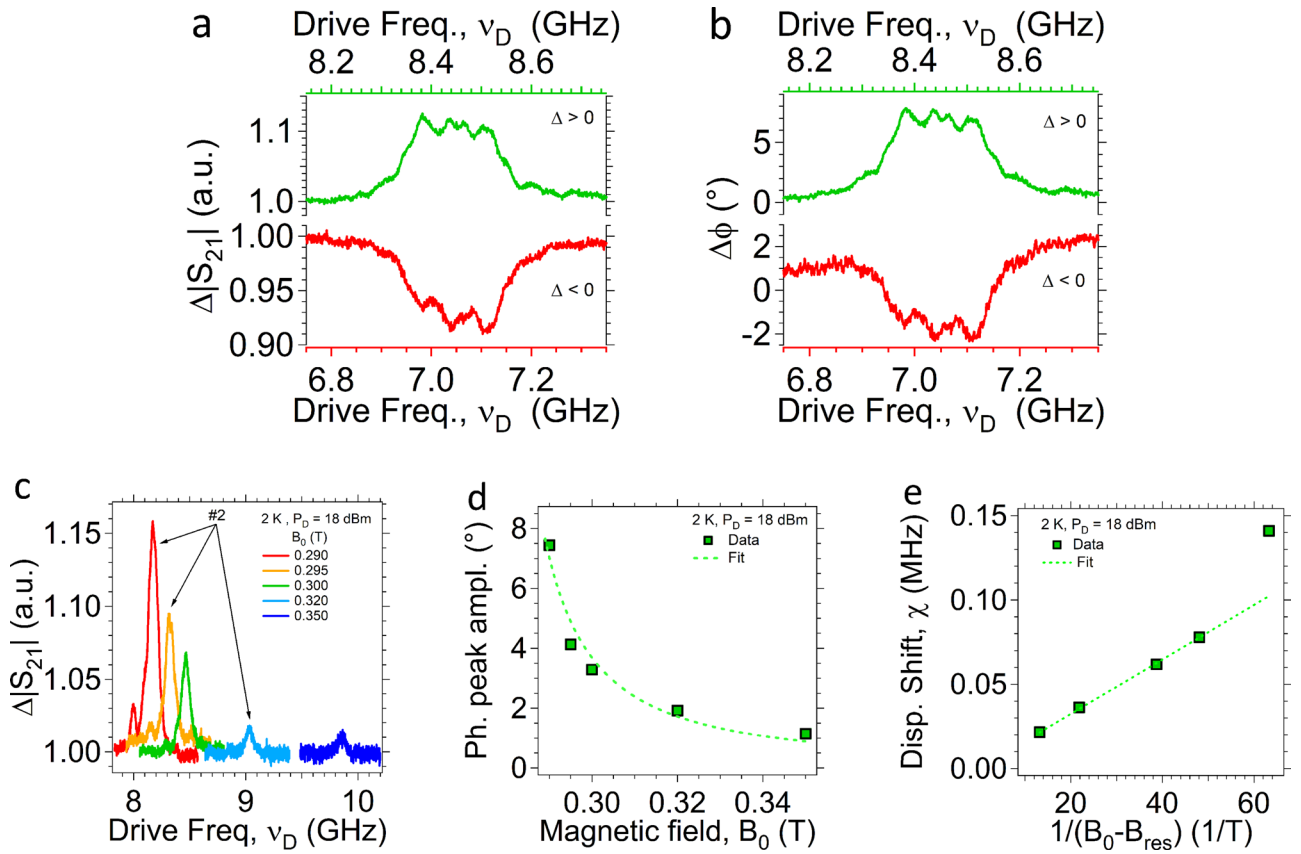

Figure 7. Top: Reversal of the shift of a) transmission and b) phase of the resonator for the 1.5% DPNO crystal at $\theta = 0°$ when the sign of the detuning is changed. Red traces and axes correspond to $B_0 = 0.2498$ T ($\Delta = -700$ MHz), while the green traces and axes correspond to $\Delta = +700$ MHz ($B_0 = 0.3000$ T, as in Figure 5). The data are taken at 2 K and using $P_{in,p} = -34$ dBm and $P_{in,D} = +18$ dBm. In each plot, the upper and the lower horizontal scales are plotted with the same step size for better comparison. The axes of each trace are plotted with the same color code. Bottom: c) Dispersive shift measured in the transmission as a function of the drive frequency for the DPNO crystal at 2 K and $\theta = 90°$ for different applied B_0. The powers are $P_{in,p} = -34$ dBm and $P_{in,D} = +18$ dBm. Black arrows with the label #2 help in following the main peak. d) Amplitude of the main peak extracted from the variation of the phase of the resonator as a function of the static magnetic field. Green dashed line is a guide for eyes. e) Dispersive shift calculated from the phase shift in (d) thanks to Equation (4) as a function of the inverse of the magnetic field difference $B_0 - B_{res}$, with B_{res} the magnetic field at which the resonance condition is met. Dashed line is a linear fit performed without considering the last point.

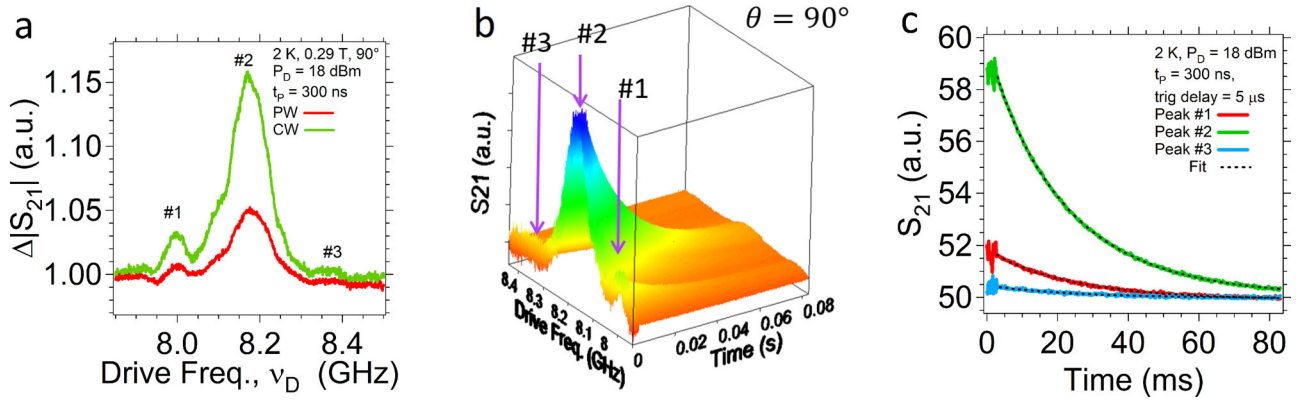

Figure 8. a) Transmission shift measured in the PW regime at 2 K (red) for the DPNO sample at $\theta = 90°$. Here $P_{in,p} = -29$ dBm and $P_{in,D} = +18$ dBm and the probe frequency is again chosen as $\nu_p = \nu_0 + \chi$. The length of the single MW drive pulse is 300 ns. Each frequency point in this plot results from a unique single-shot acquisition with the VNA. The result of the CW two-tone spectroscopy for similar field, temperature and nominal MW power is added for comparison. b) Map of the transmission of the resonator as a function of time and of the drive frequency after the application of a single 300 ns drive pulse for $\theta = 90°$, and at 2 K with $P_{in,p} = -38$ dBm and $P_{in,D} = +18$ dBm. Purple arrows with label help in identifying the dispersive signals. c) Amplitude of the three peaks of (a) and (b) as a function of time. Black dashed line is a fit obtained with Equation (9).

The results obtained for $\theta = 90°$ are shown in **Figure 8**a, along with its corresponding CW data. Note that each point of the trace results from a single-shot acquisition of the VNA. The dispersive signal shows that single driving pulses can address the spin ensemble and induce a dispersive shift on the resonator, similarly to the CW case. The comparison with the CW spectrum (green trace) shows that the position and the shape of the signal is consistent with the CW results under similar experimental conditions (in terms of temperature, applied magnetic field, MW powers). The different signal amplitudes are due to the different number of spins involved in the measurements. In fact, while for the CW case this number is set by the volume of the resonant mode (or by the residual volume of the MW field which is coupling to the spins), in the PW regime this number depends on the fraction of the spins excited by the pulse bandwidth.

3.5.1. Spin-Lattice Relaxation

Sending single MW pulses allows us to measure the spin-lattice relaxation time T_1. The sample is initially at the thermal equilibrium with the environment. The drive pulse excites a fraction of the spin population, moving the system from its equilibrium and shifting the frequency of the resonator consequently. Then the system relaxes back to thermal equilibrium according to its relaxation rate[24–26,42]

Results obtained for $\theta = 90°$ are reported in Figure 8b. The signal at $t \approx 0$ shows three main peaks (purple and labels), consistently with the one measured in CW mode for the same orientation (see Figure 8a). The signal of each dispersive peak is found to relax as expected from the recovery of the equilibrium of the resonant frequency after the initial excitation of the spins. Similar results are found measuring the phase of the resonator (see Section S8, Supporting Information). From this two-tone PW spectroscopy, the decay of the transmission of each of the three maxima (#1, #2, #3) can be extracted and plotted as a function of time (Figure 8c). Each trace fits the following exponential decay[42,56]:

$$|S_{21}(t)| = |S_{21}(t_0)|e^{-\left(\frac{t-t_0}{T_1}\right)^x} \tag{9}$$

where t_0 is the time at which the decay begins and x is the stretch factor, the latter initially left as free parameter for check. The best fit is found for $T_1 = 21 \pm 1$ ms and $x = 0.9 \pm 0.1$ at 2 K for $P_{\text{in,D}} = +18$ dBm, almost equal for all the three lines. We compare our T_1 with the values reported in [61], in which similar molecular centers and host are investigated with conventional X-band ESR. They report spin-lattice relaxation times between 6 and 10 ms on samples with concentrations (from 0.01 % to 0.2 %) lower that ours and in the intermediate temperature regime (between 50 and 180 K). Since the spin-lattice relaxation time is expected to increase with the decrease of the temperature and to decrease for increasing concentrations, we can simply conclude that our measured values are consistent with the bounds set by the data reported in the literature. However, the lack of a systemic study on the temperature dependence of the PW ESR spectra prevents us from carrying out more quantitative analyses and deeply understanding the relaxation mechanism.

4. Discussion and Conclusions

In this work, we investigated the transmission spectroscopy in the dispersive limit of the coupling between a DPNO organic radical diluted in its nonmagnetic host crystal and a coplanar microwave resonator at low temperature. Our results complement the recent reports on similar dispersive spectroscopy carried out on different spin ensembles. For instance, YIG spheres coupled to three dimensional cavities at room temperature[27] were found to give similar dependence by the detuning and by the power of the two MW tones. Likewise, the dispersive spectroscopy was found to be very powerful in estimating the zero field splitting parameters of NV-center spin ensembles[26] as well as in measuring the spin-lattice relaxation time of NV centers[25,26] and of organic radicals.[42] In our experiments, we have extended the dispersive readout to the semiclassical regime thus showing no need to work strictly under highly cooperative regime. We have also shown that the dispersive readout allows us to span over a finite frequency range around the fundamental frequency of the resonator with sufficient spectral resolution for electronic and nuclear spin transitions. The possibility to independently tune the microwave power of the two tones is an additional resource for improving the SNR. Alternatively, once the set-up is known, the noise can be tuned by adjusting the probe power when adding a controlled amount of noise into the system might be needed (e.g., for calibrations purposes).

To better assess these results, we estimate the sensitivity, S, of our resonant and dispersive spectroscopy using the relation[62]:

$$S = \frac{N_{\text{min}}}{\text{SNR}\sqrt{\text{BW}}} \tag{10}$$

Here N_{min} is the minimum number or detectable spins, SNR is the signal-to-noise ratio (see above), while BW is the acquisition bandwidth. We find $S = 3.2 \cdot 10^{12}\,\text{spin} \cdot \text{Hz}^{-1/2}$ for the single-tone (resonant) spectroscopy and $S = 8 \cdot 10^{12}\,\text{spin} \cdot \text{Hz}^{-1/2}$ for the two-tone dispersive one, respectively (see Section S9, Supporting Information, for details). Our sensitivity for the resonant case compares well with the ones reported in the literature for planar microwave resonators with comparable dimensions (although slightly larger resonant frequencies and different geometries are considered).[63,64] The sensitivity value found for the dispersive spectroscopy is only slightly smaller with respect to the corresponding resonant one (see Supporting Information for further discussion). As a benefit, the SNR can be increased by increasing the power of the probe tone without affecting the signal amplitude (under our experimental conditions), which implies that, in principle, the sensitivity in the dispersive limit might be further increased.

Since the spin ensemble is driven without a resonant mode, it is also interesting to compare our technique with on-chip single-tone broadband MW spectroscopy.[65–68] In these latter experiments a single MW tone is injected into a coplanar or a microstrip transmission line (i.e., no resonant MW modes) and used as a probe tone, to monitor the variation of the transmission induced by the ensemble. Broadband transmission spectroscopy offers large tunability of the frequency (several gigahertz), which can be used to map the energy levels of the spin ensemble as a function of the static magnetic field.[65,68] In our two-tone spectroscopy, the

dispersive shift of the cavity scales as the inverse of the detuning with respect to the probing cavity mode (Equation (3)), giving a lower tunability for the drive frequency. However, the dispersive shift depends also by the coupling rate providing that an optimal working point can be found in the tradeoff between detuning and magnetic coupling. Conversely, this cannot be done in broadband spectroscopy, also resulting in typically smaller coupling values. In addition, the background of broadband spectroscopy depends on the losses of transmission line (which mainly give a sloped baseline as a function of frequency) and on the presence of spurious resonances (e.g., box modes, magnetic impurities).[65–68] The signal given by the sample is typically obtained after the normalization of the transmission over a (carefully chosen) reference baseline taken in non-zero field. Our dispersive spectroscopy less suffers of such effects because of the following reasons: i) the resonator is typically designed to be far enough in energy with respect to box or spurious modes, ii) the smaller frequency range used gives flatter backgrounds and, iii) the signal given by eventual magnetic impurities can be naturally suppressed by the $1/\Delta$ dependence of Equation (3). As discussed in Section 3.3, the SNR can be tuned by adjusting the probe power independently by the drive tone (and not the set-up). Conversely, in the broadband spectroscopy the upper limit for the signal-to-noise is set by the control over the noise of the set-up (device and detection chain) and by the signal from the sample. While the spin sensitivity in the dispersive spectroscopy can be comparable to the one found in the resonant regime, it is reasonable to expect that using a broadband transmission line will give lower spin sensitivity.

We finally mention that the dispersive limit for positive detuning ($\Delta > 0$) implies the use of a larger drive frequency with respect to the one of the resonator. This gives a slightly increase of the energy separation of all the spectroscopic features whose energy depends on the applied static magnetic field, somehow resembling what is typically observed in high-frequency high-magnetic-field ESR. While this effect is rather small for g-factors ≈ 2, it might be more evident working with samples with larger g-factors and magnetic anisotropy (see Section S4, Supporting Information).

In conclusion, due to generality of the dispersive regime and of the dispersive readout, our results suggest that performing an electron dispersive spectroscopy can constitute a novel approach for the investigation of magnetic samples, which can be a complementary tool with respect to ESR spectroscopy.

5. Experimental Section

DPNO Samples: DPNO organic radical with 1.5% concentration in a fully deuterated benzophenone-d_{10} crystalline host was used. Each molecule had a single unpaired electron which experienced the hyperfine interaction with a nitrogen atom (nuclear spin $I = 1$), resulting in a spin $S = 1/2$ with additional split in three transitions.[61,69,70] The samples had a needle-like shape with the crystallographic c-axis corresponding to the longest side of the needle. The crystals have small magnetic anisotropy, while the hyperfine tensor results were close to a uniaxial one, with a strong component along the molecular z-axis and two much smaller ones along the x- and the y-axes, which were revealed to be approximately collinear to the crystalline ones.[61,69,70] The ESR signal of DPNO organic radicals from conventional CW X-band spectroscopy and from additional simulations was checked, and a reasonable agreement was found with our measured single-tone CW spectra. Further details of our DPNO samples are given in Section S2, Supporting Information.

Coplanar Resonator: The coplanar resonator shown in Figure 2, whose characteristics are described in details in [35, 39], was used. Briefly, the resonant strip, the side ground planes and the back ground plane were made of superconducting $YBa_2Cu_3O_7$ (YBCO) films (thickness 330 nm) on sapphire substrate (thickness $t = 430\,\mu$m). The length, $L = 8$ mm, the width, $w = 200\,\mu$m, and the gap between the resonant strip and the ground planes, $s = 73\,\mu$m, were chosen to give a fundamental resonant mode at $\nu_0 \approx 7.74$ GHz. The maximum of the MW component of the fundamental mode was located in the middle of the resonant strip, where the sample was placed (Figure 2). The resonator was mounted into a copper shielding box during the experiments, as in [35, 39]. Under our experimental conditions the resonator had a quality factor between $Q = 2000$ and $Q = 4000$ at 2 K and 0 T, depending on the position of the tunable antennas. In this work, all the input power ($P_{\text{in,p}}$ for the probe and $P_{\text{in,D}}$ for the drive) is estimated at the antenna. If not otherwise specified, the crystals were placed in order to have their c-axis in the plane of the resonator and θ will be the angle between the c-axis and the static magnetic field, as in Figure 2.

Microwave Set-Up for Dispersive Readout: The set-up used for the dispersive readout is shown in Figure 3a and it was similar to the ones previously reported in refs. [13, 27, 42]. The drive tone (frequency ν_D, power P_D) was generated by the MW source (AnaPico APSIN12G). A power amplifier (Mini-Circuits ZVE-3W-183+) with 35 dB gain can be added on the drive line to increase the drive power. A Network Analyzer (Agilent PNA 5222A Network Analyzer, VNA for short) is used for the generation of the resonator probe tone (frequency ν_p, power P_p) and the acquisition of the transmission of the resonator. On the probe line additional attenuators (Radiall R413.820.150 and R413.830.150 with 20 and 30 dB attenuation, respectively) can be added at room temperature to change the probe power. The probe and the drive signals were combined to the same MW input line with a power combiner/divider (Mini-Circuits ZN2PD2-14W-S+). The signal coming from the resonator was first filtered with two band-pass filters (Mini-Circuits VBF-7700+) to reject additional spurious mode and the eventual residual power of the drive tone, amplified (Fairview Microwave SLNA-120-38-22-SMA voltage amplifier) and finally acquired by the VNA. Additional DC Blocks (Mini-Circuits BLK-18-S+), an isolator (Raditek RADI-6.6-10.6-S3-1WR-5), and a power limiter (Pasternak PE8024), not shown in Figure 3a, were added. The whole set-up is controlled with a home-made Python software. If the MW source was turned off, the set-up allows to perform the single-tone microwave transmission spectroscopy in the resonant regime, as previously described in [39].

Typical power values used in this work were $P_{\text{in,p}} = -34 : -29$ dBm, and $P_{\text{in,D}} = 8 : 20$ dBm. These larger values for the drive tone are needed to overcome the filter effect given by the transmission lineshape of the resonator.

Protocol for the Continuous-Wave (CW) Dispersive Readout: The magnetic field was first adjusted to tune the Zeeman energy split ν_S to meet the condition for the dispersive regime $|\Delta| = |\nu_S - \nu_0| \gg \Omega$ and kept fixed during the experiment. The MW source was then used in CW mode to generate the drive tone for the spins (here, depending on the experiment performed, the drive frequency can be set to the spin energy ν_S or scanned step-by-step around it). At each frequency step of the drive, the VNA acquired both the magnitude and the phase of the transmission of the resonator. The VNA can be set to acquire the full transmission peak of the resonator or to probe the resonant peak at a fixed probing frequency close to ν_0 (in this latter case, if not otherwise specified, the conventional rule of thumb which sets the probe frequency to $\nu_p = \nu_0 + \chi$ was adopted,[71] in which the expected theoretical value according to Equation (3) was used). At the end of each scan of the drive frequency, the resonator is measured with no MW drive applied to obtain the reference transmission and phase value for the calculation of the transmission and phase shift.

Protocol for Pulsed-Wave (PW) Dispersive Readout: The microwave source is used in the PW mode to generate single MW drive pulses at ν_D and P_D and with duration t_D thanks to its internal modulator (minimum pulse duration and pulse-step increase are 30 ns). Here the trigger for the VNA acquisition is given directly by the MW source. The VNA can work in two different ways. The first one is the standard frequency mode used for the CW experiments, in which the acquisition is done in the frequency domain by probing the resonator close to ν_0. The second one is the

time-domain mode, in which the VNA acquires the signal as a function of time at a fixed probing frequency. In both these modes the VNA needed to be fast enough to follow the typical timescale of the spins dynamics. This required the use of a relatively low number of points ($\approx 500 - 1000$) for each trace and large enough bandwidths for the internal frequency ($IF \geq 10^4$) to increase the acquisition speed. The drawback was the decrease of the SNR and a loss in the trace resolution. Under the experimental conditions the minimum sweep time achievable was approximately few tens of microseconds without loosing resolution. Despite the limitations above, this configuration allowed to measure the energy relaxation of the spins, which can be identified as the spin-lattice relaxation (T_1).[24–26,42] The PW protocol used for measuring T_1 is shown in Figure 3b. At the end of each PW experiment the transmission and the phase of the resonator were acquired (in the frequency of in the time domain, depending on the VNA settings) to obtain the reference values for the calculation of the shifts.

Supporting Information

Supporting Information is available from the Wiley Online Library or from the author.

Acknowledgements

This work was partially funded by the Air Force Office of Scientific Research grant (contract no FA2386-17-1-4040) and partially by the H2020-FETOPEN "Supergalax" project (grant agreement n. 863313) supported by the European Community.

Conflict of Interest

The authors declare no conflict of interest.

Data Availability Statement

The data that support the findings of this study are available from the corresponding author upon reasonable request.

Keywords

circuit quantum electrodynamics, dispersive regime, microwaves, readout, resonance spectroscopy, spin ensembles

Received: March 10, 2021
Revised: June 8, 2021
Published online:

[1] S. Haroche, J.-M. Raimond, *Exploring the Quantum: Atoms, Cavities, and Photons*, Oxford Graduate Texts, Oxford **2006**.
[2] Z.-L. Xiang, S. Ashhab, J. Q. You, F. Nori, *Rev. Mod. Phys.* **2013**, *85*, 623.
[3] A. A. Clerk, K. W. Lehnert, P. Bertet, J. R. Petta, Y. Nakamura, *Nat. Phys.* **2020**, *16*, 257.
[4] D. Lachance-Quirion, Y. Tabuchi, A. Gloppe, K. Usami, Y. Nakamura, *Appl. Phys. Express* **2019**, *12*, 070101.
[5] I. Siddiqi, R. Vijay, M. Metcalfe, E. Boaknin, L. Frunzio, R. J. Schoelkopf, M. H. Devoret, *Phys. Rev. B* **2006**, *73*, 054510.
[6] P. Krantz, M. Kjaergaard, F. Yan, T. P. Orlando, S. Gustavsson, W. D. Oliver, *Appl. Phys. Rev.* **2019**, *6*, 021318.
[7] A. Wallraff, D. I. Schuster, A. Blais, L. Frunzio, R.-S. Huang, J. Majer, S. Kumar, S. M. Girvin, R. J. Schoelkopf, *Nature* **2004**, *431*, 162.
[8] A. Wallraff, D. I. Schuster, A. Blais, L. Frunzio, J. Majer, M. H. Devoret, S. M. Girvin, R. J. Schoelkopf, *Phys. Rev. Lett.* **2005**, *95*, 060501.
[9] J. Gambetta, A. Blais, D. I. Schuster, A. Wallraff, L. Frunzio, J. Majer, M. H. Devoret, S. M. Girvin, R. J. Schoelkopf, *Phys. Rev. A* **2006**, *74*, 042318.
[10] R. Vijay, D. H. Slichter, I. Siddiqi, in *2011 IEEE MTT-S Int. Microwave Symp.*, IEEE, Baltimore, MD, USA **2011**, https://doi.org/10.1109/MWSYM.2011.5972726.
[11] T. Walter, P. Kurpiers, S. Gasparinetti, P. Magnard, A. Potočnik, Y. Salathé, M. Pechal, M. Mondal, M. Oppliger, C. Eichler, A. Wallraff, *Phys. Rev. Applied* **2017**, *7*, 054020.
[12] D. I. Schuster, A. A. Houck, J. A. Schreier, A. Wallraff, J. M. Gambetta, A. Blais, L. Frunzio, J. Majer, B. Johnson, M. H. Devoret, S. M. Girvin, R. J. Schoelkopf, *Nature* **2007**, *445*, 515.
[13] A. Schneider, J. Braumüller, L. Guo, P. Stehle, H. Rotzinger, M. Marthaler, A. V. Ustinov, M. Weides, *Phys. Rev. A* **2018**, *97*, 062334.
[14] A. Crippa, R. Ezzouch, A. Aprá, A. Amisse, R. Laviéville, L. Hutin, B. Bertrand, M. Vinet, M. Urdampilleta, T. Meunier, M. Sanquer, X. Jehl, R. Maurand, S. De Franceschi, *Nat. Commun.* **2019**, *10*, 2776.
[15] P. Scarlino, D. J. van Woerkom, A. Stockklauser, J. V. Koski, M. C. Collodo, S. Gasparinetti, C. Reichl, W. Wegscheider, T. Ihn, K. Ensslin, A. Wallraff, *Phys. Rev. Lett.* **2019**, *122*, 206802.
[16] A. J. Landig, J. V. Koski, P. Scarlino, C. Müller, J. C. Abadillo-Uriel, B. Kratochwil, C. Reichl, W. Wegscheider, S. N. Coppersmith, M. Friesen, A. Wallraff, T. Ihn, K. Ensslin, *Nat. Commun.* **2019**, *10*, 5037.
[17] A. A. Houck, D. I. Schuster, J. M. Gambetta, J. A. Schreier, B. R. Johnson, J. M. Chow, L. Frunzio, J. Majer, M. H. Devoret, S. M. Girvin, R. J. Schoelkopf, *Nature* **2007**, *449*, 328.
[18] M. Hofheinz, E. M. Weig, M. Ansmann, R. C. Bialczak, E. Lucero, M. Neeley, A. D. O' Connell, H. Wang, J. M. Martinis, A. N. Cleland, *Nature* **2008**, *454*, 310.
[19] B. R. Johnson, M. D. Reed, A. A. Houck, D. I. Schuster, L. S. Bishop, E. Ginossar, J. M. Gambetta, L. DiCarlo, L. Frunzio, S. M. Girvin, R. J. Schoelkopf, *Nat. Phys.* **2010**, *6*, 663.
[20] K. Inomata, Z. Lin, K. Koshino, W. D. Oliver, J.-S. Tsai, T. Yamamoto, Y. Nakamura, *Nat. Commun.* **2016**, *7*, 12303.
[21] S. Kono, K. Koshino, Y. Tabuchi, A. Noguchi, Y. Nakamura, *Nat. Phys.* **2018**, *14*, 546.
[22] D. Lachance-Quirion, Y. Tabuchi, S. Ishino, A. Noguchi, T. Ishikawa, R. Yamazaki, Y. Nakamura, *Sci. Adv.* **2017**, *3*, e1603150.
[23] J. Ebel, T. Joas, M. Schalk, P. Weinbrenner, A. Angerer, J. Majer, F. Reinhard, *Quantum Science and Technology*, IOP Publishing, Bristol, UK **2021**.
[24] A. Angerer, K. Streltsov, T. Astner, S. Putz, H. Sumiya, S. Onoda, J. Isoya, W. J. Munro, K. Nemoto, J. Schmiedmayer, J. Majer, *Nat. Phys.* **2018**, *14*, 1168.
[25] V. Ranjan, G. de Lange, R. Schutjens, T. Debelhoir, J. P. Groen, D. Szombati, D. J. Thoen, T. M. Klapwijk, R. Hanson, L. DiCarlo, *Phys. Rev. Lett.* **2013**, *110*, 067004.
[26] R. Amsüss, C. Koller, T. Nöbauer, S. Putz, S. Rotter, K. Sandner, S. Schneider, M. Schramböck, G. Steinhauser, H. Ritsch, J. Schmiedmayer, J. Majer, *Phys. Rev. Lett.* **2011**, *107*, 060502.
[27] J. A. Haigh, N. J. Lambert, A. C. Doherty, A. J. Ferguson, *Phys. Rev. B* **2015**, *91*, 104410.
[28] K. Bader, D. Dengler, S. Lenz, B. Endeward, S.-D. Jiang, P. Neugebauer, J. Van Slageren, *Nat. Commun.* **2014**, *5*, 5304.
[29] J. M. Zadrozny, J. Niklas, O. G. Poluektov, D. E. Freedman, *ACS Cent. Sci.* **2015**, *1*, 488.
[30] M. Atzori, L. Tesi, E. Morra, M. Chiesa, L. Sorace, R. Sessoli, *J. Am. Chem. Soc.* **2016**, *138*, 2154.
[31] R. Sessoli, M. Atzori, L. Sorace, S. Carretta, A. Chiesa, E. Morra, M. Chiesa, *Chem. Sci.* **2018**, *9*, 6183.

[32] M. Atzori, R. Sessoli, *J. Am. Chem. Soc.* **2019**, *141*, 29 11339, pMID: 31287678.
[33] E. Macaluso, M. Rubín, D. Aguilà, A. Chiesa, L. A. Barrios, J. I. Martínez, P. J. Alonso, O. Roubeau, F. Luis, G. Aromí, S. Carretta, *Chem. Sci.* **2020**, *11*, 10337.
[34] F. Troiani, A. Ghirri, M. Paris, C. Bonizzoni, M. Affronte, *J. Magn. Magn. Mater.* **2019**, *491*, 165534.
[35] A. Ghirri, C. Bonizzoni, D. Gerace, S. Sanna, A. Cassinese, M. Affronte, *Appl. Phys. Lett.* **2015**, *106*, 184101.
[36] A. Ghirri, C. Bonizzoni, F. Troiani, N. Buccheri, L. Beverina, A. Cassinese, M. Affronte, *Phys. Rev. A* **2016**, *93*, 063855.
[37] M. Mergenthaler, J. Liu, J. J. Le Roy, N. Ares, A. L. Thompson, L. Bogani, F. Luis, S. J. Blundell, T. Lancaster, A. Ardavan, G. A. D. Briggs, P. J. Leek, E. A. Laird, *Phys. Rev. Lett.* **2017**, *119*, 147701.
[38] C. Bonizzoni, A. Ghirri, M. Atzori, L. Sorace, R. Sessoli, M. Affronte, *Sci. Rep.* **2017**, *7*, 13096.
[39] C. Bonizzoni, A. Ghirri, M. Affronte, *Adv. Phys.: X* **2018**, *3*, 1435305.
[40] C. Bonizzoni, A. Ghirri, F. Santanni, M. Atzori, L. Sorace, R. Sessoli, M. Affronte, *npj Quantum Inf.* **2020**, *6*, 68.
[41] T. Fan, V. I. Tsifrinovich, A. D. Kent, *Phys. Rev. B* **2011**, *84*, 024410.
[42] A. K. Keyser, J. J. Burnett, S. E. Kubatkin, A. V. Danilov, M. Oxborrow, S. E. de Graaf, T. Lindström, *J. Magn. Reson.* **2020**, *321*, 106853.
[43] S. Yamamoto, S. Nakazawa, K. Sugisaki, K. Sato, K. Toyota, D. Shiomi, T. Takui, *Phys. Chem. Chem. Phys.* **2015**, *17*, 2742.
[44] T. Yoshino, S. Nishida, K. Sato, S. Nakazawa, R. D. Rahimi, K. Toyota, D. Shiomi, Y. Morita, M. Kitagawa, T. Takui, *J. Phys. Chem. Lett.* **2011**, *2*, 449.
[45] Y. Tabuchi, S. Ishino, A. Noguchi, T. Ishikawa, R. Yamazaki, K. Usami, Y. Nakamura, *C. R. Phys.* **2016**, *17*, 729.
[46] Y. Tabuchi, S. Ishino, A. Noguchi, T. Ishikawa, R. Yamazaki, K. Usami, Y. Nakamura, *Science* **2015**, *349*, 405.
[47] M. Tavis, F. W. Cummings, *Phys. Rev.* **1969**, *188*, 692.
[48] D. Lachance-Quirion, S. P. Wolski, Y. Tabuchi, S. Kono, K. Usami, Y. Nakamura, *Science* **2020**, *367*, 425.
[49] I. Chiorescu, N. Groll, S. Bertaina, T. Mori, S. Miyashita, *Phys. Rev. B* **2010**, *82*, 024413.
[50] J. H. Wesenberg, A. Ardavan, G. A. D. Briggs, J. J. L. Morton, R. J. Schoelkopf, D. I. Schuster, K. Mølmer, *Phys. Rev. Lett.* **2009**, *103*, 070502.
[51] T. Holstein, H. Primakoff, *Phys. Rev.* **1940**, *58*, 1098.
[52] S. Miyashita, T. Shirai, T. Mori, H. D. Raedt, S. Bertaina, I. Chiorescu, *J. Phys. B: At., Mol. Opt. Phys.* **2012**, *45*, 124010.
[53] A. Imamoğlu, *Phys. Rev. Lett.* **2009**, *102*, 083602.
[54] D. Zueco, G. M. Reuther, S. Kohler, P. Hänggi, *Phys. Rev. A* **2009**, *80*, 033846.
[55] M. Stammeier, S. Garcia, T. Thiele, J. Deiglmayr, J. A. Agner, H. Schmutz, F. Merkt, A. Wallraff, *Phys. Rev. A* **2017**, *95*, 053855.
[56] A. Abragam, B. Bleaney, *Electron Paramagnetic Resonance of Transition Ions*, Oxford Classics Texts in the Physical Sciences, Oxford **2012**.
[57] G. Boero, G. Gualco, R. Lisowski, J. Anders, D. Suter, J. Brugger, *J. Magn. Reson.* **2013**, *231*, 133.
[58] E. Abe, H. Wu, A. Ardavan, J. J. L. Morton, *Appl. Phys. Lett.* **2011**, *98*, 251108.
[59] T. Astner, J. Gugler, A. Angerer, S. Wald, S. Putz, N. J. Mauser, M. Trupke, H. Sumiya, S. Onoda, J. Isoya, J. Schmiedmayer, P. Mohn, J. Majer, *Nat. Mater.* **2018**, *17*, 313.
[60] N. Abhyankar, A. Agrawal, P. Shrestha, R. Maier, R. D. McMichael, J. Campbell, V. Szalai, *Sci. Adv.* **2020**, *6*, eabb0620.
[61] C. Cheng, T.-S. Lin, D. J. Sloop, *J. Magn. Reson.* **1979**, *33*, 71.
[62] A. Blank, Y. Twig, Y. Ishay, *J. Magn. Reson.* **2017**, *280*, 20.
[63] R. Narkowicz, D. Suter, R. Stonies, *J. Magn. Reson.* **2005**, *175*, 275.
[64] R. Narkowicz, D. Suter, I. Niemeyer, *Rev. Sci. Instrum.* **2008**, *79*, 084702.
[65] C. Clauss, D. Bothner, D. Koelle, R. Kleiner, L. Bogani, M. Scheffler, M. Dressel, *Appl. Phys. Lett.* **2013**, *102*, 162601.
[66] M. D. Jenkins, Y. Duan, B. Diosdado, J. J. García-Ripoll, A. Gaita-Ariño, C. Giménez-Saiz, P. J. Alonso, E. Coronado, F. Luis, *Phys. Rev. B* **2017**, *95*, 064423.
[67] A. Ghirri, C. Bonizzoni, M. Righi, F. Fedele, G. Timco, R. Winpenny, M. Affronte, *Appl. Magn. Reson.* **2015**, *46*, 749.
[68] I. Gimeno, A. Urtizberea, J. Román-Roche, D. Zueco, A. Camón, P. J. Alonso, O. Roubeau, F. Luis, *Chem. Sci.* **2021**, *12*, 5621.
[69] T. S. Lin, *J. Chem. Phys.* **1972**, *57*, 2260.
[70] J. Yamauchi, H. Nishiguchi, K. Mukai, Y. Deguchi, H. Takaki, *Bull. Chem. Soc. Jpn.* **1967**, *40*, 2512.
[71] A. Sokolov, *Phys. Rev. A* **2016**, *93*, 032323.